Chapter 5
Integrated Studies of Au@Pt and Ru@Pt Core-Shell Nanoparticles by *In Situ* Electrochemical NMR, ATR-SEIRAS, and SERS

Dejun Chen, Dianne O. Atienza, and YuYe J. Tong

5.1 Introduction

Nanoscale noble metal materials, mostly in the form of nanoparticles (NPs), have been subjected to intensive research in the context of their applications to fuel cell electrocatalysis [1] traditionally and also to lithium-air batteries [2, 3] recently. Among others, despite decades-long continuous efforts in discovering viable replacements for the expensive and earthly-scant platinum (Pt), Pt-based electrocatalysts [4, 5] are still the materials of choice in terms of having high activity for CO oxidation reaction (COR) [6, 7], methanol oxidation reaction (MOR) [8], ethanol oxidation reaction (EtOR) [9, 10], formic acid oxidation reaction (FAOR) [11, 12], hydrogen evolution/oxidation reaction (HER/HOR) [13, 14], oxygen reduction/evolution reaction (ORR/OER) [15–17], and CO_2 reduction reaction (CO_2R) [18, 19], just to name a few widely studied reactions. Benefited from the fertile knowledge gained from the decades-long intensive investigations of model electrocatalysts, such as single crystal surfaces, fundamental research on discovering, understanding and utilizing novel electronic, geometric, and/or bifunctional properties of Pt-based NPs [20–22] for the aforementioned reactions continues to flourish and push the boundary of research in an environment as close to that of practical applications as possible. Constant advance of the sophistication of many *in situ* spectroelectrochemical techniques has been a critical part of the latter. In this Chapter, we will discuss integrated studies of Au@Pt and Ru@Pt NPs by *in situ* electrochemical (EC) nuclear magnetic resonance (NMR), attenuated-total-reflection surface-enhanced IR reflection adsorption spectroscopy (ATR-SEIRAS), and surface-enhanced Raman scattering spectroscopy (SERS)

D. Chen • D.O. Atienza • Y.Y.J. Tong (✉)
Department of Chemistry, Georgetown University, 37th and O Streets, NW, Washington, DC 20057, USA
e-mail: yyt@georgetown.edu

spectroscopy, with a focus on how an organic integration of these techniques can enhance the investigative power brought to bear by their complementary nature. That is, an organically integrated whole is better than the sum of its parts.

The strength of NMR is in its unique ability to probe the electronic and structural properties of Pt-based NPs [23]. Particularly, ^{195}Pt NMR can distinguish, at least semi-quantitatively, the Pt atoms on the surface of from those inside the NPs and the Pt atoms in metallic from non-metallic (e.g. oxidized) state [24, 25]. Moreover, using adsorbed ^{13}CO as a molecular probe, ^{13}C NMR can offer complementary electronic and diffusional information of the surface [26–28]. However, NMR continues to suffer from its intrinsic low mass detection sensitivity so it is generally not a method of choice for detecting reaction intermediates during the reaction. On the other hand, SEIRAS and SERS are more suited for the latter [29, 30].

Since its inception [31], EC-SEIRAS has been applied extensively to study electrocatalysis mainly on conductive metal thin-films (~50 to 100 nm thick) used as working electrodes [32]. Single metallic films, such as Au [32–34], Pt [35–43], Pd [44, 45], Cu [46], Ag [47], and bimetallic PtRu [43, 48], PtPd [44] alloy film as well as additional ultrathin-film (bi)metallic layers deposited on Au substrate film [49, 50], have been the subjects of studies of COR [34, 41], MOR [40, 42, 43, 48], EtOR [36], FAOR [39, 44, 45, 50], HER/HOR [35, 38], ORR [51, 52] and CO_2R [37]. Numerous surface species that are important to the reactions under investigation, such as adsorbed CO (CO_{ads}) in linearly/bridge/multiple bonding configurations [37, 43, 45, 50], formate [39, 40, 45, 53], adsorbed anion [33, 45] and interfacial water [32, 54, 55], have been identified and studied [30]. On the other hand, while SERS may not be as versatile and sensitive as SEIRAS, EC-SERS does offer some complementary advantages, such as observing species that only have symmetric vibrational modes, for instance O_2^- [56], accessing to lower wavenumber range (100~1000 cm^{-1}) in which the vibrations of metal-adsorbate, such as Pt-CO [57] or Pt-O [58], locate and not worrying about strong absorption by water. With the enhancement offered by roughened bulk surfaces [29, 59] or deposited NPs [60–62], EC-SERS has become increasingly used to study catalytic reactions, such as COR [57, 60, 63, 64], MOR [57, 65], FAOR [62], ORR [56] and H_2O_2 electro-reduction reaction [66, 67], on the respective electrocatalyst surface.

Despite their complementary nature, EC-NMR, -SEIRAS or -SERS has been largely used alone for various reasons. But an integrated approach of combining them together to investigate the same system is expected to provide a fuller mechanistic picture of the system under investigation. With this in mind, and as already briefly mentioned above, we will focus here on two samples, Ru@Pt and Au@Pt NPs, which have been studied in various degree of detail by *in situ* EC-NMR, -SEIRAS, and -SERS. This chapter will be structured as follows: we will first present briefly the physical aspects of the samples (Sect. 5.2), then move to NMR (Sect. 5.3), SEIRAS (Sect. 5.4), and SERS (Sect. 5.5) sequentially, which will be followed by an integrated discussion (Sect. 5.6) of the results presented in the previous sections. We will conclude the chapter with some summative comments.

5.2   Ru@Pt and Au@Pt NPs Samples

Ru@Pt NPs. The synthesis was adopted from the wet homogeneous reaction-like procedure developed by Du et al. [68]. Briefly, the ethylene glycol (EG) was used as both reaction medium and reducing agent of Johnson-Matthey (J-M) Ru Black (~3 nm) and $H_2PtCl_6 \cdot 6H_2O$. The first step is the complete reduction of Ru NPs at 140 °C for 2 h with vigorous stirring. This step is critical for the success of controlling the surface Pt deposition where it has been determined experimentally that Ru readily oxidizes to RuO_x in the atmosphere [69]. The cleaned Ru NPs were then collected and rinsed with ethanol and re-dispersed ultrasonically into a fresh EG solution. The calculated volume of $H_2PtCl_6 \cdot 6H_2O$ solution according to the experimentally determined linear relationship [68] gave the desired ≈40 % Pt packing density (PD). This mixture was ultrasonicated and heated at 120 °C for 4 h to reduce Pt(IV) to Pt(0) on the surface of cleaned Ru NPs. This synthetic method in a lower temperature homogeneous-reaction like media is advantageous in preventing sintering effects. A representative TEM image is shown in Fig. 5.1a from which the average particle size was determined to be 3.2 nm.

Au@Pt NPs. Au colloid NPs (3.5 nm) were first prepared from $HAuCl_4 \cdot 3H_2O$ in aqueous solution using sodium citrate and sodium borohydride as reductant and then supported spontaneously on Vulcan XC-72R that gave a metal loading of 30 wt %. The Pt shell was deposited by reducing Pt^{4+} onto the surface of dispersed carbon-supported Au NPs by using ascorbic acid with target Pt coverage of 100 % (atomic ratio of Pt/Au = 1). The detail of the synthesis can be found in the original paper [70]. A representative TEM image is shown in Fig. 5.1b that gives an average particle size of 4.6 nm.
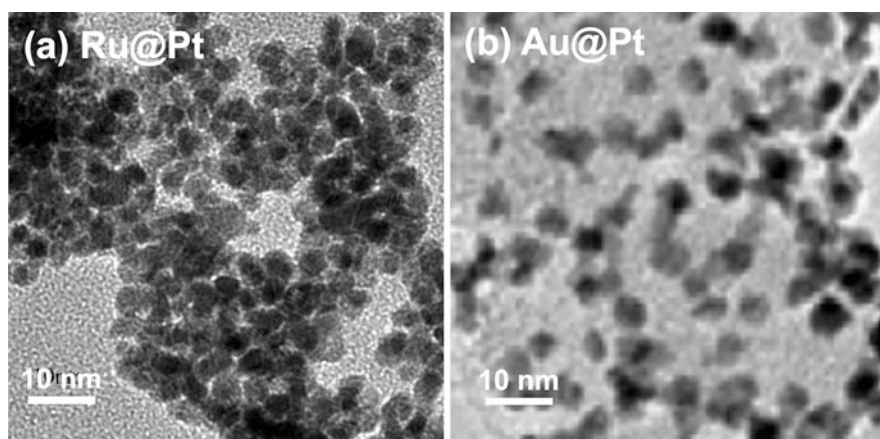

Fig. 5.1 TEM images of Ru@Pt (**a**) and Au@Pt (**b**). The average particle size is 3.2 nm for the former and 4.6 nm for the latter. (**b**) is adapted with permission from [70] (© 2007 Elsevier)

5.3 *In Situ* EC-NMR Study of Ru@Pt and Au@Pt NPs [71]

For EC-NMR measurements, the NMR samples (~50–80 mg) were treated at room temperature by an EC cleaning process in a three-electrode setup with the NPs as working electrode by holding the potential at 50 mV (vs. Ag/AgCl). For CO adsorption from dissociation of ^{13}C-labeled methanol (^{13}C-MeOH) onto the pre-clean NPs surface was done with the same cell but in 0.1 M $HClO_4$ + 0.5 M MeOH solution by holding the potential at 250 mV. The EC setup was under a continuous stream of ultrapure Argon gas during the entire period of the above treatments. After the EC cleaning or CO adsorption, the NMR sample cell filled with the supporting electrolyte (0.1 M $HClO_4$ or 0.1 M $HClO_4$ + 0.5 M ^{13}C-MeOH) was sealed immediately with a one-to-one fitted ground-glass stopper, which was then inserted into the NMR probe and lowered down to the cryostat that was pre-cooled at 80 K. After the NMR measurements, the cell was immediately reconnected back to the EC cleaning setup. The open-circuit potential was re-checked to make sure that its stability was within a 20 mV difference before and after the NMR measurements. The ^{13}C NMR spectra of the adsorbed [13]CO and the corresponding inversion-recovery spin-lattice T_1 measurements were obtained at various temperature ranges of 80–120 K at a "home-assembled" spectrometer equipped with an active-shielded 9.395 T widebore superconducting magnet, an Oxford Spectrostat-CF cryostat (Oxford Instrument, U.K.), an AMT (Lancaster, PA) 1 kW power amplifier, a Tecmag (Houston, TX) Apollo data acquisition system, and a home-built single channel solenoid probe with a coil of 5 mm inner diameter and 28 mm length. Both the ^{13}C and [195]Pt spectra were acquired using the conventional "$\pi/2$-τ-π-τ-echo" Hahn spin-echo sequence with the $\pi/2$ pulse length and τ of 3 μs and 25 μs respectively but for the [195]Pt spectra the frequency was manually changed between ca. 82–87 MHz with a 0.047 G/kHz increment between each resonance position at 80 K because of the extremely broadness of the spectra. The slow beats of the [195]Pt signal at a given frequency (see Fig. 5.2e, f) are obtained by varying the τ in the spin-echo sequence and the corresponding T_1 measurements were done with the conventional saturation-recovery method.

Figure 5.2a, b shows the point-by-point [195]Pt NMR spectra of the as-received (red) and EC-cleaned (blue) samples of Au@Pt (with Pt packing density (PD) = 3.8, A) and of Ru@Pt (with Pt PD = 0.4, D) core-shell NPs in comparison with that of the pure Pt/C NPs [73] (black dashed lines and open circles). The vertical dashed line indicates the surface peak position (1.1000 G/kHz,) of the EC-cleaned pure 2.5 nm Pt/C NPs [73]. Although the frozen electrolyte at 80 K prevented active potentiostatic control, the tightly vacuum-sealed sample cell ensured that the sample surface potential would not change during the NMR measurements. This was verified by measuring open circuit potentials before and after each NMR measurement that always indicated that a constant potential was indeed achieved.

The as-received Au@Pt NPs had a shelf life of more than 48 months [70], therefore, the surface was heavily oxidized, as indicated by the peak of Pt oxide at 1.089 G/kHz (Fig. 5.2a). Notice that distinguishing a Pt surface covered by
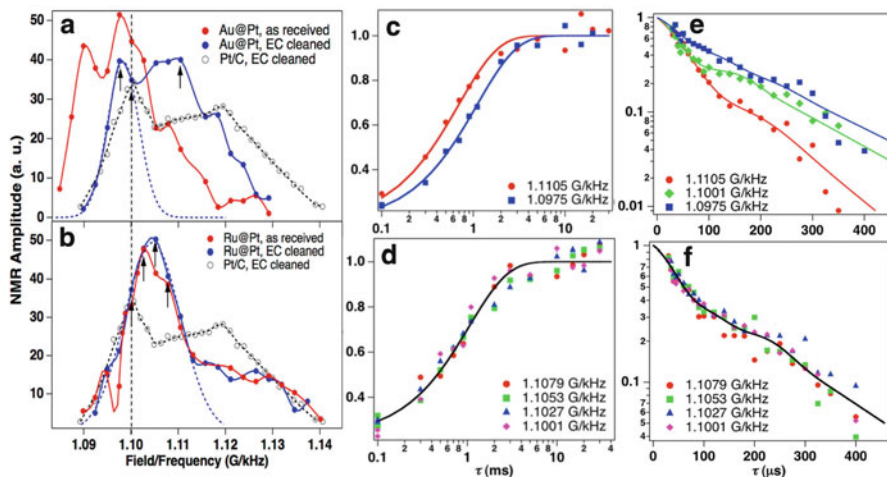
Fig. 5.2 Point-by-point ^{195}Pt NMR spectra (**a**, **b**), spin–lattice relaxation curves (**c**) and (**d**), spin-spin relaxation (*J*-coupling modulation or slow-beat) curves (**e**, **f**) for the Au@Pt (**a**, **c**, **e**) and Ru@Pt (**b**, **d**, **f**) NPs, respectively. The calculated Pt PD (packing density) was 3.8 for the Au@Pt and 0.4 for the Ru@Pt NPs. According to the straight line in Fig. 3 of [72], the expected Pt surface fraction would be 1.3, i.e., a fully Pt covered Au core. The % of the total deposited Pt on the surface would be ~1.3/3.8 = 0.34, in an excellent agreement with the value of 33 % determined by ^{195}Pt NMR in a. Adapted from [71] with permission (© 2012 American Chemical Society)

adsorbed oxygen from that by Pt oxide is straightforward. After the EC cleaning, the Pt oxide peak disappeared and a clean-surface peak appeared at 1.0975 G/kHz. The latter amounts to a 2278-ppm *positive* shift with respect to the clean-surface peak position (1.1000 G/kHz) of the pure Pt NPs, manifesting a strong electronic effect of Au on Pt. The significant portion of the ^{195}Pt atoms in the Au@Pt NPs resonating at higher fields (above 1.1000 G/kHz) indicates that many deposited Pt atoms went inside the Au NPs. Indeed, using a Gaussian de-convolution of the surface peak (the dashed blue curve in Fig. 5.2a), we found that only ≈33 % of all Pt deposited atoms were on the surface of the Au@Pt NPs, which is in agreement with expected atomic exchange between deposited Pt atoms and the underlying Au atoms [72]. Notice that such a ~33 % value is actually predicted by the straight line in Fig. 3 of [72] (see caption of Fig. 5.2).

The as-received Ru@Pt NPs were freshly synthesized with a shelf life of only a few hours [68]. Under the protection of ethylene glycol, little surface oxidation was expected in such a short time. Indeed, no significant surface oxidation was observed in the corresponding ^{195}Pt NMR spectrum in Fig. 5.2b (red). The clean-surface peak (blue line) now appeared at 1.1053 G/kHz, corresponding to a 4795-ppm *negative* shift with respect to the clean-surface peak position (1.1000 G/kHz) of the pure Pt NPs, revealing also a strong electronic effect of Ru on Pt as well, which is *opposite* to that of Au. A Gaussian de-convolution of the surface peak gave a surface atom fraction of ≈74 %, indicating a dominant Ru core Pt shell structure.

The nuclear spin-lattice (T_1) and spin-spin (T_2) relaxation measurements are presented in Fig. 5.2c, e for the EC-cleaned Au@Pt and in 2d and 2f for the EC-cleaned Ru@Pt, respectively, at the spectral positions listed in the respective figures. Detailed discussion of the relaxation results is out of scope here due to the limited space, but it suffices to demonstrate the most important difference here. Both the T_1 (Fig. 5.2d) and T_2 (Fig. 5.2f) at different spectral positions on the Ru@Pt fall into the *same* respective relaxation curves, which is a manifestation of the same chemical environment, i.e., the majority of the Pt atoms were on the surface. Particularly, a *J*-coupling modulation analysis [25] of the data in Fig. 5.2f by fitting to the J-coupling induced slow beats equation [74] $S(\tau)/S_0 = \exp(-2\tau/T_2)$ $(P_0 + \exp(-(\tau/T_{2J})^2)[P_1\cos(J\tau) + P_2\cos^2(J\tau)])$ with J for J-coupling constant, $1/T_{2J}$ for spread in J, and $P_0 + P_1 + P_2 = 1$ (solid line) gives a Pt atomic fraction of 0.37. Since for a full pseudo-morphic Pt monolayer on a Ru(0 0 0 1) surface, the Pt atomic fraction among all the possible next nearest neighbors is $6/9 = 0.67$, a local Pt atomic fraction of 0.37 is thus consistent with a Pt PD of 0.4 of mono-atomic Pt islands. In contrast, both the T_1 (Fig. 5.2c) and T_2 (Fig. 5.2e) at different spectral positions on the Au@Pt were different, which indicates a wider distribution of Pt atoms on surface and inside the NPs as well.

From the T_1 value, the known spectral position and temperature at which the T_1 is measured, one can use the two-band model to calculate the *s*- and *d*-like E_f–LDOSs, denoted here as $D_s(E_f)$ and $D_d(E_f)$ respectively [75]. These values for the surface Pt atoms in Au@Pt and Ru@Pt samples are collected in Table 5.1. *As can be clearly seen*, *Au and Ru cores exert different* (*opposing*) *electronic influence on Pt shell*: *the former lowers more the d-like while the latter lowers more the s-like E_f–LDOSs.*

Also collected (in the parentheses) in Table 5.1 are the average surface values calculated by using the OpenMX DFT package [76] on Pt13@Pt42 (Pt55), Ru13@Pt42, and Au13@Pt42 cubo-octahedral clusters. Considering the very simplified cluster models, it is remarkable that the experiments and theoretical calculations have achieved a good agreement in numerical values and in trend for both $D_s(E_f)$ and $D_d(E_f)$.

How changes in the surface Pt *s*- and *d*-like E_f-LDOS induced by the Au and Ru cores influence metal-adsorbate bonding was probed and corroborated by ^{13}C NMR of [13]CO adsorbed onto the Au@Pt and Ru@Pt NPs via dissociative adsorption of [13]CH$_3$OH (MeOH). The ability to probe the surface electronic properties by

Table 5.1 E_f-LDOS values deduced from [195]Pt and ^{13}C NMR data (1 Ry = 13.6 eV and mol = molecule)

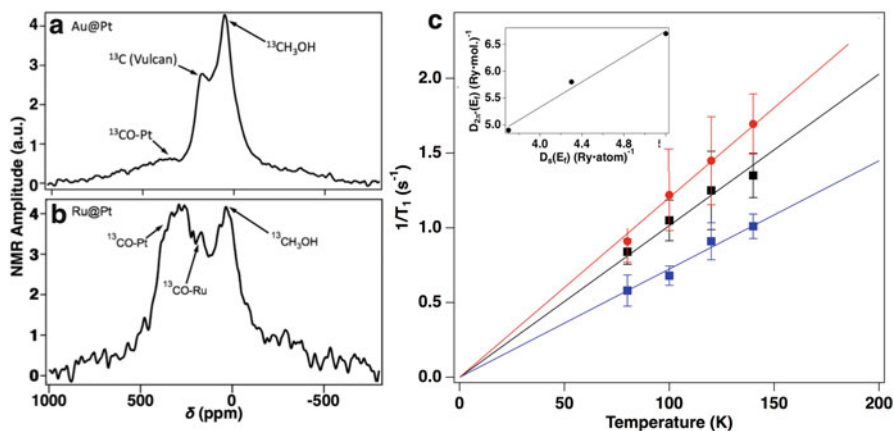| Samples	$D_s(E_f)$/Ry^{-1} atom^{-1}	$D_d(E_f)$/Ry^{-1} atom^{-1}	$D_5\sigma(E_f)$/Ry^{-1} mol^{-1}	$D_2\pi_*(E_f)$/Ry^{-1} mol^{-1}
Ru@Pt	3.7 (2.9)	13.3 (12.9)	0.7	4.9
Au@Pt	4.3 (3.0)	10.1 (12.7)	0.6	5.8
Pt	5.1 (3.4)	13.5 (15.2)	0.7	6.7

Fig. 5.3 ^{13}C NMR spectra (9.39 T, 80 K) of chemisorbed CO on (**a**) Au@Pt and (**b**) Ru@Pt NPs. Electro-deposition of CO was performed by holding the potential at 0.35 V vs. Ag/AgCl (3 M) while immersed in 0.5 M D_2ClO_4 with [13]CH_3OH [13]. CH_3OH at 49 ppm was also used as an internal shift reference. (**c**) Temperature dependent T_1 relaxation measurements obtained at 333 ppm for CO-Pt/Ru@Pt and CO-Pt/Au@Pt and at 219 ppm for CO-Ru/Ru@Pt. Adapted from [71] with permission (© 2012 American Chemical Society). Inset in (**c**): Linear correlation between the $D_2\pi_*(E_f)$ and $D_s(E_f)$

using surface-adsorbed molecules, such as adsorbed [13]CO, is among the unique investigative strengths of *in situ* EC-NMR. Figure 5.3 shows the ^{13}C NMR spectra of [13]CO on the Au@Pt (a) and Ru@Pt (b) NPs, with the assigned peaks indicated by the arrows. For the Au@Pt sample, despite the dominant peaks from the remaining MeOH in the electrolyte and the carbon support, the broad and weak—yet still discernable—^{13}C NMR peak at ≈333 ppm was assigned to the adsorbed CO, an assignment corroborated by the temperature dependent T_1 measurements (*vide infra*). For the Ru@Pt sample, the peaks at ≈300 ppm and ≈219 ppm can be assigned to CO on Pt and on Ru sites, respectively, based on the literature values [27, 77]. *The difference in the signal strength of the adsorbed CO on the Au@Pt and Ru@Pt NPs may reflect the difference in dissociative adsorption of MeOH on the respective surfaces.*

The results of temperature dependent T_1 measurements are presented in Fig. 5.3c. For the CO on Pt, the T_1's were measured at 333 ppm for both Au@Pt ($T_1T = 83$ s K) and Ru@Pt ($T_1T = 99$ s K) samples to facilitate comparison, although the peak position for the latter was at ≈ 300 ppm. The pass-through-origin straight lines are the hallmark of the Korringa relaxation behavior [78], which indicates that the adsorbed CO molecules on three different sites all acquired metallic characteristics through surface bonding. For CO on Ru sites, the shift (219 ppm) and Korringa constant $T_1T = 138$ s K (where T is the absolute temperature at which T_1 is measured) are very close to those observed on pure Ru [77] and on Ru deposited on Pt NPs [27], which lends strong support to our peak assignment that is also consistent with the expected exposure of Ru core for a Pt PD of 40 %. On

the other hand, the Korringa constants measured at the same spectral position (333 ppm) were different for CO on the surface Pt atoms of the Au@Pt and on those of the Ru@Pt NPs. The former showed a faster relaxation (i.e., smaller Korringa constant T_1T), and thus a stronger metal-adsorbate bonding. In fact for CO on Pt, we can also deduce the values of the respective 5σ- and 2π*-like E_f–LDOS, i.e., $D_5\sigma(E_f)$ and $D_{2\pi*}(E_f)$, at ^{13}C by using a different two-band model developed for adsorbed CO on Pt [26].

As can be seen from the data in Table 5.1, the $D_{5\sigma}(E_f)$ was essentially constant, while the $D_{2\pi*}(E_f)$ decreased proportionally (inset in Fig. 5.3c) with the $D_s(E_f)$ for CO on Pt from pure Pt to Au@Pt to Ru@Pt. This suggests that the electronic alterations on metal-CO bonding, i.e., changes in metal to CO 2π* back-donation [79], and therefore in bonding strength, were mainly caused by the variations in the $D_s(E_f)$ of the surface Pt atoms. On the other hand, it has been observed that the ability to dissociatively adsorb MeOH that leads to adsorbed CO follows the order $Pt \approx Ru@Pt > Au@Pt$, which shares the same order in the respective $D_d(E_f)$ as shown in Table 5.1. These results suggest that the *d*-like electrons are probably responsible for agostic interaction that activates the three methyl protons in MeOH during its dissociative adsorption.

5.4   *In Situ* EC ATR-SEIRAS of Ru@Pt and Au@Pt NPs [80]

Figure 5.4 shows the schematic of the EC IR cell that was used for *in situ* EC ATR-SEIRAS measurements of the Ru@Pt and Au@Pt samples. A gold film was first electrolessly deposited onto the reflecting plane of a Si attenuation total reflection (ATR) prism of a triangular shape, which was polished with successively
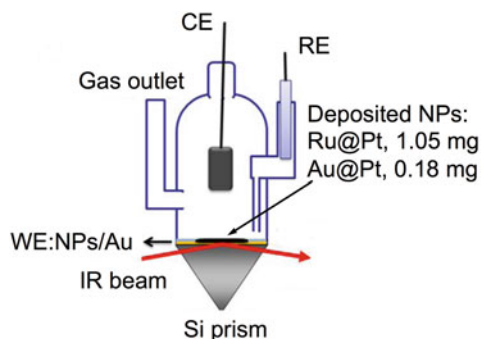

Fig. 5.4   Schematic of the *in situ* EC ATR-SEIRAS cell used for ATR-SEIRAS measurements. WE, RE and CE stand for working, reference and counter electrode respectively. A ~50-nm Au film was first deposited onto the pre-polished Si prism onto which the Ru@Pt or Au@Pt NPs were then drop-casted and dried with nitrogen flow

finer grade alumina slurries down to 0.3 μm and cleaned by sonication in the Milli-Q water. The detailed deposition procedure can be found elsewhere [81].

For the *in situ* EC-SEIRAS measurements, Ru@Pt (1.05 mg) and Au@Pt/C (0.18 mg) were dispersed onto the as-prepared gold film. The catalytic adlayer of the core-shell NPs was then dried in a gentle nitrogen flow at room temperature. No Nafion® solution was used in order to avoid any optical interference. The working electrode surface (Au film plus NPs) was cleaned by repetitive potential cycling until stable and reproducible cyclic voltammograms (CV) were achieved in 0.1 M $HClO_4$ at 50 mV s^{-1} between −0.3 V and 0.7 V for the Ru@Pt, and −0.25 V and 1.0 V for the Au@Pt/C NPs, respectively. Notice that the Ru@Pt had an expected Pt PD or coverage of 40 % while that for the Au@Pt was 100 %.

Figure 5.5a, b present the SEIRAS spectra of two sequential COR potential scans after gaseous CO adsorption on the Ru@Pt (a-1 and a-2) and the Au@Pt (b-1 and b-2) NPs. The reference spectra were taken at 0.7 V for the former and 1.0 V for the latter at which all adsorbed CO had been fully oxidized according to the corresponding CO stripping voltammograms. While the same IR band of linearly-bound CO-Pt was observed on the Au@Pt NPs for the two sequential COR runs (Fig. 5.5b, d), there were changes for the CO spectra on the Ru@Pt NPs. In (a-1), the spectra show a series of a *single*, potential-dependent CO IR band that varied between 1998 and 2047 cm^{-1}, which can be assigned to a linearly-bonded CO_L [43, 82]. The peak position of this single band at −0.15 V (spectrum (a) in the inset of Fig. 5.5c) is 2005 cm^{-1}, a value in agreement with those of CO adsorbed on the Ru sites of Ru-decorated Pt(1 1 1) surfaces (from 2001 to 2008 cm^{-1}) [82–84] but between those of CO_L on pure Ru (~1995 cm^{-1}) [43, 82] and on PtRu alloy (~2044 cm^{-1}) [43, 85] under the similar conditions. For CO absorbed on the Ru-modified Pt(1 1 1) surfaces, two distinct CO stretching bands corresponding to Pt-CO_L and Ru-CO_L respectively were observed; but on the Ru@Pt of the first COR in this study and on PtRu alloys [43, 85, 86] in general, only one band was observed.

On the other hand, the SEIRAS spectra obtained between −0.3 to 0.3 V of the CO during the second COR on the Ru@Pt can be reasonably de-convoluted into three peaks whose values at −0.15 V are 1948 cm^{-1}, 2000 cm^{-1} and 2031 cm^{-1} respectively (spectrum b in the inset of Fig. 5.5c). Based on the available literature values and assignments of the C-O stretching frequencies of adsorbed CO on Ru [43], Ru-decorated Pt [82, 83, 87], and PtRu alloy [43, 88, 89] surfaces, we assigned the three peaks to CO_L bonded to Ru-coordinated-to-Ru (or Ru sites distal to the Pt islands–Ru-like sites, 1948 cm^{-1}), Ru-coordinated-to-Pt (or Ru sites proximal to the Pt islands–PtRu sites, 2000 cm^{-1}), and Pt-islands-on-Ru-core (or Pt adlayer sites that are most close to Pt sites in PtRu alloys–Pt-like sites, 2031 cm^{-1}) sites on the surface of the Ru@Pt NPs respectively. The middle-frequency sites are most likely around the peripheries of the Pt islands formed on the surface of Ru core [90].

Because Ru is highly oxophilic, the exposure of the Ru@Pt NPs to air after the synthesis can easily lead to an enrichment of Ru species to the surface [91]. Moreover, neither repetitive CVs between −0.3 V and 0.7 nor holding electrode potential at −0.3 V could readily modify such a Ru enrichment on the surface of the Ru@Pt NPs. Consequently, only one C-O stretching band (Fig. 5a-1) similar to that of
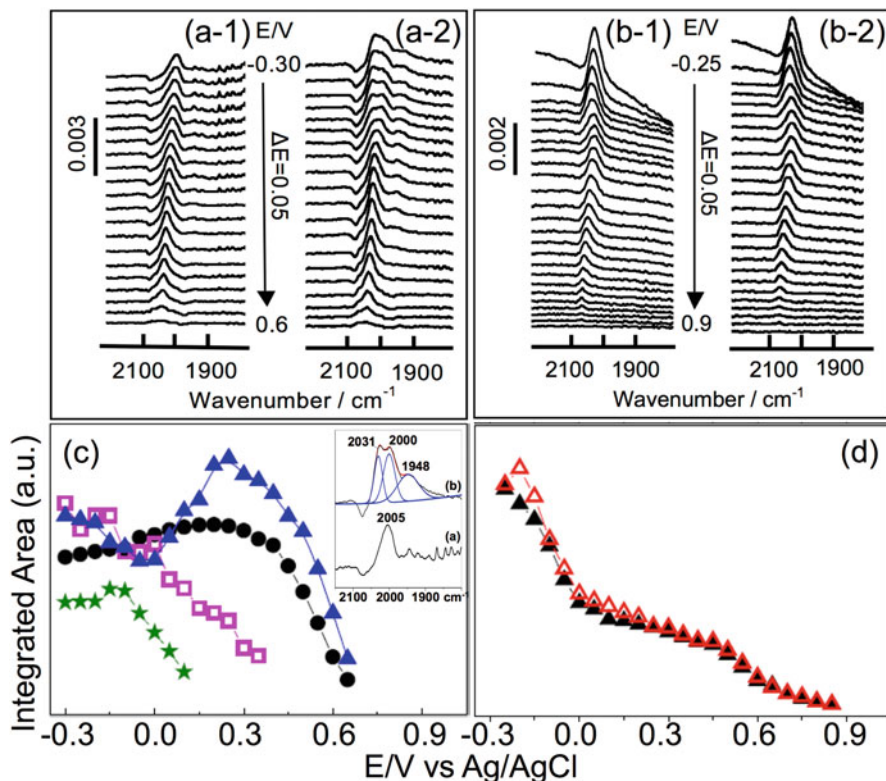
Fig. 5.5 The potential dependent EC-SEIRAS spectra of the pre-adsorbed CO during the first (**a-1/b-1**) and the second (**a-2/b-2**) COR on the Ru@Pt/Au@Pt/C NPs respectively in 0.1 M HClO$_4$. The spectra taken at 0.7 V for the Ru@Pt and 1.0 V for the Au@Pt/C were used as the corresponding reference spectra. The integrated areas of the spectra in (**a**) and (**b**) are plotted in (**c**) and (**d**) respectively. The inset in (**c**) compares fine spectral features of (**a-1**) and (**a-2**) taken at −0.15 V. The spectra in (**a-2**) can be de-convoluted into three bands: 2031-cm^{-1} (*green stars*), 2000-cm^{-1} (*blue triangles*) and 1948-cm^{-1} (*pink squares*) bands, which should be compared with those in (**a-1**) where only one band (2005 cm^{-1}, *black circles*) was observed. In contrast, only one same IR band that varied between 2025 and 2070 cm^{-1} was observed in (**b-1**, *black triangles* in **d**) and (**b-2**, *red triangles* in **d**). Adapted from [80] with permission (© 2011 American Chemical Society)

CO$_L$-Ru of Ru-modified Pt(1 1 1) surface [82] was observed, suggesting a dominant CO-Ru species on the surface.

On the other hand, the first COR acted like a CO annealing process and was able to reduce (at least partially) the surface Ru oxide (RuO$_x$ or RuO$_x$H$_y$) to metallic Ru and to bring the segregated Pt sites back to the surface of the Ru@Pt NPs so that CO could adsorb onto different surface sites that led to the appearance of the three different C-O stretching peaks as observed in the inset of Fig. 5.5c. The potential dependent integrated IR band intensity of each de-convoluted band is presented in Fig. 5.5c. What is intriguing is that the integrated intensity of each band behaves

differently. The 2031-cm^{-1} band (the Pt-islands-on-Ru-core sites, green stars) shows the most negative onset potential of the COR, i.e., ~−0.1 V, at which the CO IR intensity starts decreasing. The 2000-cm^{-1} band (the Ru sites proximal to the Pt islands, blue solid triangles) shows little intensity changes from −0.3 to 0.0 V, a noticeable intensity increase from 0.0 to 0.25 V, and then a rapid intensity decease beyond 0.25 V. The latter can be considered the COR onset potential of these sites. Lastly, the CO IR intensity of the 1948-cm^{-1} band (the Ru sites distal to the Pt islands) decreases slowly until ~0.15 V beyond which a shaper decrease starts. Thus, 0.15 V can also be considered as its COR onset potential.

The above observations led us to conclude that, in terms of the COR, the Pt-islands-on-Ru-core sites were the most active; the proximal Ru sites were the least active, and the distal Ru sites were in between. Although these differences in the reaction rate of the COR may reflect differences in reaction barrier and/or CO diffusion rate at these sites, their relatively lower onset potentials for the COR should be contrasted to that of the first COR whose value is about 0.35 V (Fig. 5.5c, black circles). This indicates that the more segregated surface structures of the Ru@Pt NPs generated by the CO annealing, i.e., Pt islands on metallic Ru core, is much more active than the (largely ruthenated) surface structure before the CO annealing of which surface Ru oxides dominated, an observed was further confirmed by our recent study of the chemistry related to the activation of commercial PtRu alloy electrocatalysts [92].

Figure 5.5b-1 and b-2 depict the potential dependent EC-SEIRAS spectra for the two sequential CORs on the Au@Pt/C NPs. As briefly mentioned above and in contrast to the cases of the Ru@Pt NPs presented in Fig. 5.5a-1 and a-2, no obvious differences were observed in terms of the SEIRAS of the pre-adsorbed CO between the two sequential CORs, as can been seen in Fig. 5.5b, d: only one CO IR stretching band varying from 2025 to 2070 cm^{-1} was observed over the entire potential range, which can be assigned to a linearly bonded CO_L-Pt. This infers rather constant surface structure and properties of the Au@Pt/C, an indication of stability.

What is puzzling but also intriguing is the rather precipitous decrease in the IR intensity below 0.0 V where adsorbed CO is supposed to be stable. Coincidently, the potential dependence of the vibrational frequency in this region also behaved oddly (not shown here but can be consulted in the original paper [80]). Since the linearly increasing current during CO stripping positive-going potential scan was largely negative in this potential regime [80], we speculated that an ongoing protonation-like process converted adsorbed CO into a different species whose exact identity is still unknown. However, the species-conversion hypothesis is consistent with the observation of the non-monotonic frequency variation observed in the same potential regime mentioned above [93] and with the observation of co-adsorbed hydrogen on Pt electrodes by visible-infrared SFG [94] and by SEIRAS [95–98]. Moreover, if this large decrease in IR intensity were caused by a much earlier COR, it would be hard to reconcile with that no enhanced MOR was observed on the Au@Pt NPs as will be discussed below.
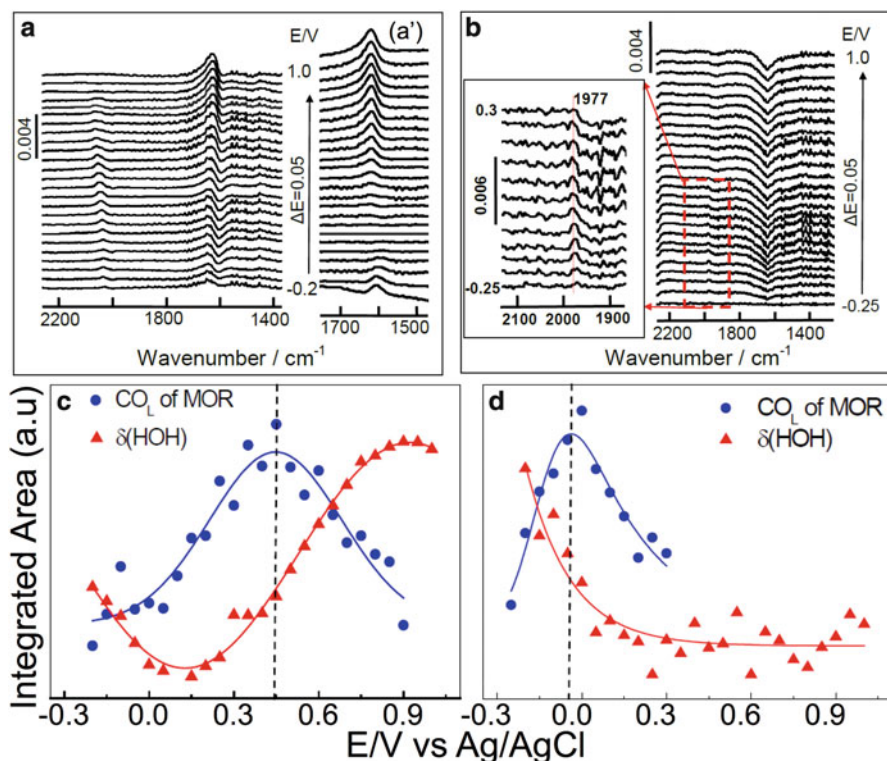
Fig. 5.6 The *in situ* SEIRAS spectra acquired in 0.5 M MeOH + 0.1 M HClO$_4$ during positive potential scan of MOR on the Au@Pt (**a** and **a'**) and Ru@Pt (**b**) NPs, with the spectra taken at −0.25 and −0.3 V as the respective references. The spectra in (**a'**) are the water bending bands for the Au@Pt/C NPs obtained using the spectrum recorded at 0.1 V as the reference while the inset in (**b**) amplifies the very weak CO spectra. (**c**) and (**d**) show the corresponding potential dependent integrated IR intensity of the adsorbed CO$_L$ (*blue*) and the surface water bending δ(HOH) (*red*). The *solid lines* are for eye-guiding purpose. Adapted from [80] with permission (© 2011 American Chemical Society)

The MOR on the Ru@Pt and Au@Pt/C NPs after the two sequential CORs discussed above was followed by the *in situ* stair-step potential dependent EC-SEIRAS in 0.5 M MeOH + 0.1 M HClO$_4$. On the Au@Pt/C NP surface a weak Pt-CO$_L$ band around 2040 cm^{-1} was observed as shown in Fig. 5.6a whose corresponding integrated intensity is shown in Fig. 5.6c (solid blue circles). Notice that while the COR of the pre-adsorbed gaseous CO (Fig. 5.5b) started with a fully CO-covered surface, the MOR started with a CO free surface. Therefore, the increase in IR intensity of the CO$_L$ during the MOR before 0.45 V is a manifestation of the accumulation of the surface-bound poisonous CO generated from the dissociative adsorption of MeOH. Notice that the CO intensity started decreasing at 0.45 V, which is consistent with the main-current peak potential of the CO stripping [80].

During the potential dependent MOR, a somewhat bipolar water bending vibration δ(HOH) band was observed at ~1620 cm^{-1} with the negative going signal appearing at the lower frequency side. If the spectra were re-referenced by the spectrum obtained at 0.1 V, the original bipolar spectral shape largely disappeared (Fig. 5.6a'). This is because 0.1 V is around the potential of zero charge, PZC [99], at which IR bending vibration of the absorbed water is expected to be weakest [32]. The now dominantly mono-polar spectra in Fig. 5.6a' reveals a more clear trend: The peak intensity decreased first gradually and the bending frequency moved from 1608 cm^{-1} at -0.2 V to 1600 cm^{-1} just below 0.1 V; it then started increasing continuously with a constant bending frequency at 1622 cm^{-1} above 0.1 V (red triangles in Fig. 5.6c). Such a behavior of the δ(HOH) is very similar to that observed on Pt film [95], which was interpreted as due to changes in the hydrogen-bonding-associated average orientation of water molecules with oxygen-up or down on the negative or positive charged Pt surface separated by the PZC.

Below the PZC, the Au@Pt/C NP surface was negatively charged so it attracted the hydrogen end of the water molecules. As the electrode potential became less negative, the attraction to hydrogen became weaker, so less hydrogen-down water molecules would bond to the surface and led to weaker IR intensity of the water-bending band. As the electrode potential moved further positively beyond the PZC, the Au@Pt/C NP surface became more and more positively charged, leading to attracting more and more water molecules via the oxygen-end of the water molecules. Consequently, the IR intensity of the water-bending band became stronger. Although the electro-oxidation of MeOH and adsorbed CO must have consumed surface water, the continuous increase in water adsorption above 0.1 V indicates that the MOR on the Au@Pt/C NPs was overall slow. The oxidation of the surface above 0.75 V led to the observed level-off and then decrease in the IR intensity.

The band of the adsorbed CO generated during the MOR on the Au@Pt/C NPs was much weaker than the pre-adsorbed gaseous CO for the COR. This is consistent with the EC results that showed the degree of the suppression of hydrogen adsorption was much lower for the former than that for the latter. Yet, an even weaker linearly bound CO band at about 1977 cm^{-1} (at -0.05 V) was observed for the MOR on the Ru@Pt NPs, whose integrated intensity, although about three times smaller than that of the CO generated during the MOR on Au@Pt NPs, followed the same increase-then-decrease pattern with the peak at -0.05 V (Fig. 5.6d). It is highly likely that this CO band corresponds to the poisonous CO generated during the MOR on the Pt-islands-on-Ru-core sites, for the Ru sites are essentially inactive for MOR. Moreover, this onset is almost identical with that of CO_L on Pt islands of Ru@Pt for second COR (green stars in Fig. 5.5c). The very low CO coverage was probably responsible for the significant red shift in stretching frequency from the full-coverage value of ~2030 cm^{-1} to the low-coverage value of 1977 cm^{-1}.

Notice that the MOR generated CO-band peak potential of -0.05 V for the Ru@Pt NPs was 0.5 V more negative than that (0.45 V) for the Au@Pt/C NPs. This observation implies a much less CO poisoning and faster MOR on the Ru@Pt than on the Au@Pt/C NPs. Indeed, the amplitude of the corresponding surface water

bending vibration δ(HOH) band at 1641 cm^{-1} (Fig. 5.6b) did not show an increase after 0.1 V but instead reached a constant level (Fig. 5.6d), signaling that the MOR on the Ru@Pt NPs was much faster than on the Au@Pt/C NPs such that it led to a higher rate of surface water consumption, therefore a steady state of surface water adsorption.

As activated surface water is a necessary surface reactant for both COR and MOR [100, 101], its *in situ* IR spectroscopic investigation has proven informative and revealing [7, 41, 102]. The IR vibrational frequency, band shape, and intensity of the surface water at the EC interface are very sensitive to several parameters that include the type of metal surface, the strength and direction of interfacial electric field, and the co-adsorbed species. In addition to the bending mode δ(HOH) discussed above, three distinguishable ν(O-H) stretching bands of interfacial water have been identified and reported: [32, 95, 103, 104] the non-hydrogen bonded water monomer at ~3660 cm^{-1}, the strongly hydrogen-bonded ice-like water at ~3040 cm^{-1}, and the disordered weakly hydrogen-bonded water at ~3400 cm^{-1}.

For the MOR, two water bands were observed (Fig. 5.7a): the weakly hydrogen-bonded at 3380 cm^{-1} and strongly hydrogen-bonded at 3075 cm^{-1}. Their potential dependent, integrated IR intensity obtained by peak de-convolution are presented in Fig. 5.7b. The initial intensity decrease in both bands can be again rationalized by the reduced attraction to the hydrogen of the water molecule as the surface became
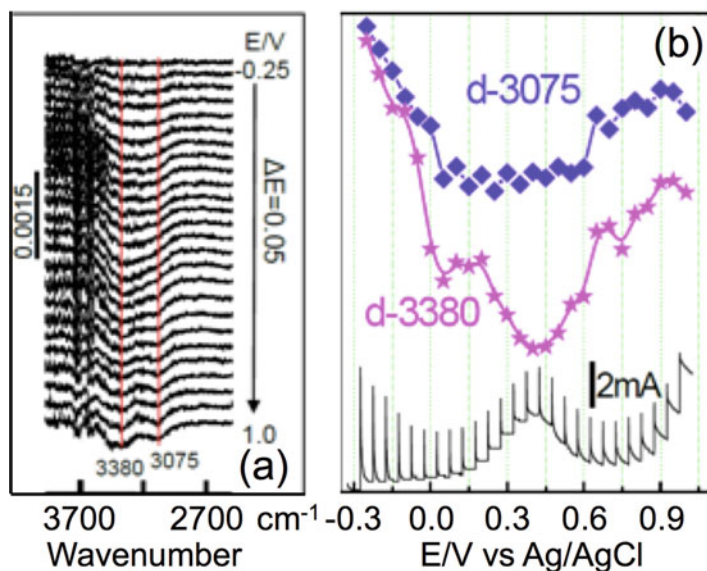

Fig. 5.7 (**a**) The potential dependent EC-SEIRAS spectra of the ν(O-H) bands observed on the Ru@Pt NPs during MOR and (**b**) the corresponding integrated IR intensity of the 3380-cm^{-1} (*pink stars*) and 3075-cm^{-1} (*blue diamonds*) bands as indicated by the *vertical red lines* in (**a**). Also presented in (**b**) is the current transient recorded during the stair-step IR measurements (*black curve with spikes*). Adapted from [80] with permission (© 2011 American Chemical Society)

less negatively charged. The second large decrease in the integrated intensity for the weakly hydrogen-bonded water at 3380 cm^{-1} that peaked at ~0.45 V as compared to the flat amplitude of the strongly hydrogen-bonded water band at 3075 cm^{-1} over the same potential region strongly suggests that the former type of water was at least more actively involved in the MOR and therefore was consumed more. This activity correlation is further supported by the simultaneously recorded current transients over the potential-step changes (black curve in Fig. 5.7b). The clear overlap of the MOR current peak with the IR intensity dip of the weakly hydrogen-bonded water is the strongest experimental evidence showing that the weakly hydrogen-bonded water was the active water species for the MOR on the Ru@Pt NPs.

The *in situ* EC-SEIRAS spectra of the ν(O–H) band of the interfacial water on the Au@Pt/C NPs during the COR in 0.1 M HClO$_4$ and MOR in 0.1 M HClO$_4$ + 0.5 M MeOH are presented in Fig. 5.8a, b. Very similar behaviors were observed for both cases, consisting of a broad band at 3245 cm^{-1} with a shoulder at ~3400 cm^{-1} over the entire potential range studied. Additionally, a small yet visible and also narrower peak at ~3580 cm^{-1} was observed for potentials more positive than ~0.3 V for the COR and than ~−0.1 V for the MOR, respectively. The potential dependent integrated band intensities obtained via de-convolution were plotted in Fig. 5.8c, d (the blue circles for the COR and red triangles for the MOR) for the 3435-cm^{-1} (weakly hydrogen-bonded) and 3245-cm^{-1} (strongly hydrogen-bonded) water bands, respectively.
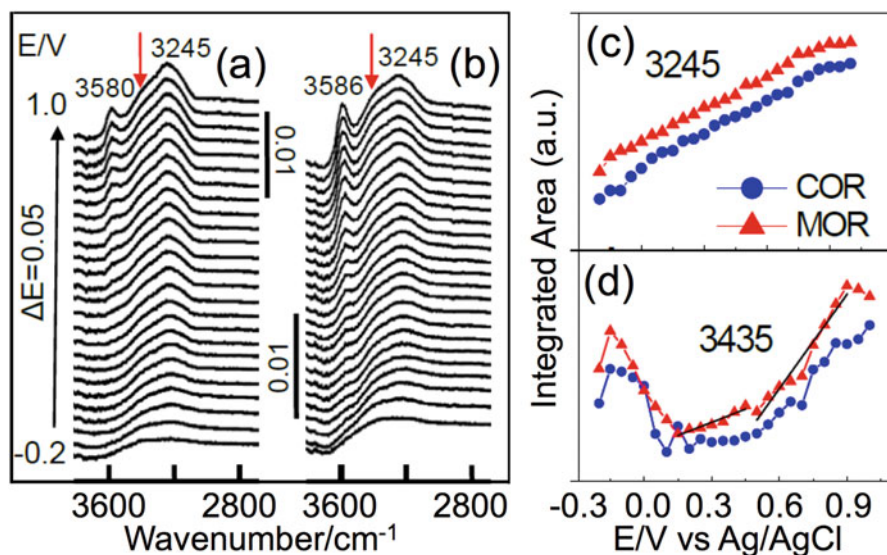

Fig. 5.8 Potential dependent EC-SEIRAS spectra of ν(O-H) stretch vibration for the Au@Pt/C NPs during the COR (**a**) and MOR (**b**). The integrated IR intensity of the 3245-cm^{-1} (**c**) and 3580-cm^{-1} (**d**) bands as a function of potential for the COR (*blue circle*) and MOR (*red triangle*) obtained by spectral de-convolution. Adapted from [80] with permission (© 2011 American Chemical Society)

Among the three different types of water observed, only the weakly hydrogen-bonded water in both the COR and MOR (Fig. 5.8d) show a variation pattern in the potential-dependent, integrated IR band intensity that has three different potential regimes: −0.25 to 0.1 V, 0.1–0.45 V, and 0.45–1.0 V, which closely match those of IR band of the adsorbed CO (Fig. 5.5d). Interestingly, two distinct increasing rates of the IR intensity were observed in the latter two potential regimes: 0.28, 0.12 a.u./ V below and 1.01, 0.79 a.u./V above ~0.45 V (see the black straight lines in Fig. 5.8d) for MOR and COR, respectively, of which the electrode potential of 0.45 V coincides with the peak potential of the COR and the poisonous CO generated during the MOR (Fig. 5.6c). Thus, the much bigger increasing rate of the IR intensity above 0.45 V is most likely due to the oxidation of adsorbed CO_L in COR and MOR that rendered more surface sites available for water adsorption. Such a pattern match strongly suggests that the weakly hydrogen-bonded water species most likely occupied the surface sites freed by the CO oxidation and might also be the source of oxygen-containing species for the COR and MOR as suggested by the observations made on the Ru@Pt NPs (Fig. 5.7b), although more direct evidence supporting this assignment is still needed. Moreover, since no $v(OH)$ band corresponding to adsorbed $Pt-OH_{ads}$ (~3700 cm^{-1}) [103] was observed during both the COR and MOR and on both samples, the dissociative adsorption of water on Pt ($Pt-OH_2 \rightarrow Pt-OH_{ads} + H^+ + e^-$) was probably the rate-determining step for both the COR and MOR [7].

5.5 *In Situ* SERS of Pt and Ru@Pt

Figure 5.9 shows the Schematic of our *in situ* EC-SERS cell. The cell body is made of Teflon with a quartz window through which the laser is shined onto the surface of working electrode, which can be a rough Au film electrode, a roughened Pt disk electrode, or NPs deposited on the substrate electrode. For the current study, commercial Pt black or the synthesized Ru@Pt NPs were drop-casted onto a normal Pt disk electrode from which Raman signal is too weak to be observed. The surface enhancement came from the NPs themselves but it was time-consuming to locate a "hot" spot. For the measurements, 0.1 M $HClO_4$ or 0.1 M $HClO_4$ + 0.5 M MeOH were used for COR and MOR respectively. The EC-SERS spectra were obtained using a confocal Raman microscope system (Renishaw RM1000) equipped with a deep depletion CCD peltier cooled down to −70 °C. The microscope attachment is based on an Olympus BH2-UMA system and uses a ×50 objective. A holographic notch filter was used to filter the excitation line, and 1200 g mm^{-1} selective holographic grating was employed depending on the spectral resolution required. The excitation wavelength was 785 nm from a Renishaw diode laser with a maximum power of 100 mW. For each spectrum, exposure time was 120 s; each potential step was held for 253 s during the *in situ* EC SERS measurements.

Figure 5.10 compares the *in situ* EC SERS spectra of the adsorbed CO at −0.25 and 0.0 V acquired during COR and MOR on Pt black and Ru@Pt respectively. It shows
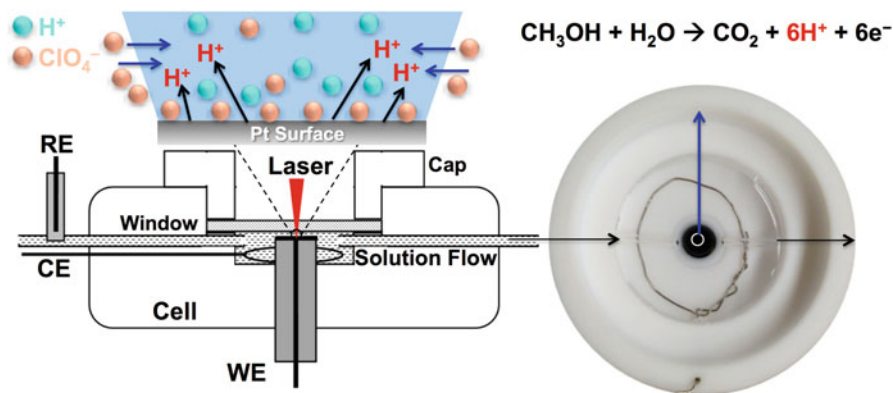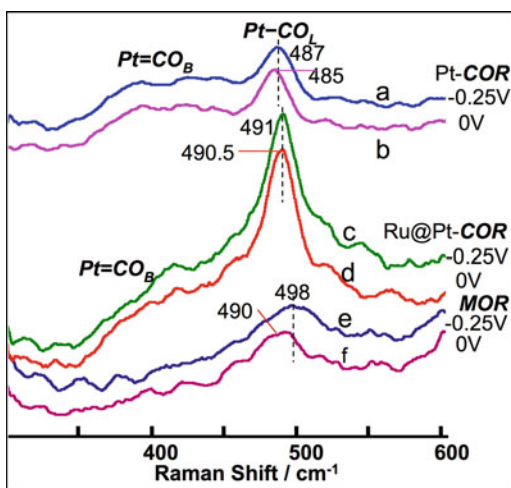
Fig. 5.9 The schematic of the *in situ* EC SERS cell with a photo of the working electrode encased in the cell body as seen from the top. Adapted from [93] with permission (© 2014 Royal Society of Chemistry)

Fig. 5.10 *In-situ* EC SERS spectra of the bonding of Pt–CO$_{ads}$ during the COR (**a–d**) and MOR (**e, f**) at −0.25 and 0.0 V on the Pt black and the Ru@Pt NPs

that the gaseous adsorption generated Pt–CO bands on Pt and Ru@Pt at 0.0 V appeared at 485 cm^{-1} and 490.5 cm^{-1}, respectively, with a difference of ~+5 cm^{-1}. On the other hand, the v(C–O) on Pt and Ru@Pt at the same potential presents bands at 2052 cm^{-1} and 2006 cm^{-1}, respectively, with a difference of ~−46 cm^{-1}. In other words, in contrast to the large red shift (~−46 cm^{-1}) for C-O stretching on pure Pt vs on Ru@Pt, the corresponding difference in the Pt–CO vibrational frequency shows a small but still significant blue shift (~+5 cm^{-1}). Such opposing shifts in $v_{Pt–CO}$ vs $v_{C–O}$ indicates that the addition of Ru makes the Pt sites more electron-accepting or having higher Lewis acidity [105]. For MeOH generated CO on the Ru@Pt, the band intensity was much weaker, indicating improved CO tolerance. But it also showed the largest negative Stark tuning slope: −32 cm^{-1}/V (the other two were

much smaller though still negative). That the SERS can access ν_{Pt-CO} vibration, which is directly related to metal–CO bonding and inaccessible to IR, offers insight that is complementary to the intra-molecular vibration that can be measured by IR.

5.6 Discussion

In the above sections, we have presented *in situ* EC [195]Pt and [13]CO NMR, SEIRAS and SERS data obtained on the same Ru@Pt and Au@Pt NPs, shedding light on different aspects of their respective electrocatalytic behaviors. For instance, NMR probes the electronic properties of the metal NPs, IR exams the intra-molecular vibrations and by which identifies reaction intermediates, and Raman accesses to the metal–adsorbate vibrations. Altogether, they can provide a fuller picture and deeper understanding of the system under investigation.

NMR's ability to provide quantitative information on electronic partition at the Fermi level (Table 5.1) can be of good use to connect with some recent theoretical development. For instance, recent quantum calculations on oxide-supported Pt model systems [106] have (re-) unearthed a potentially important and also more chemically intuitive surface bonding descriptor–the electronic partition, i.e., 6sp vs 5d electrons, at Pt that has been less (if not at all) investigated in electrocatalysis. The calculations predict that the Pt–H bond would be stronger at a Pt site with higher 6sp partition, while the Pt–O bond would be stronger at a Pt site with higher 5d partition, with Pt–CH$_3$ and Pt–CH$_2$ in between. The relatively recent application of the *C*rystal *O*rbital *H*amiltonian *P*opulation (COHP) formalism [107] within the extended Hückel *m*olecular *o*rbital (MO) theory to chemisorption of CO, hydrogen, methyl, and ethyl to metal surfaces by Hoffman and co-workers [108] also highlight the revealing power of such a chemistry-based *e*lectronic-*o*rbital-*s*pecific (EOS) formalism. For instance, the COHP analysis revealed that the metal *sp* orbitals actually contribute significantly (much more than previously believed) to the overall CO-Ni and CO-Pt chemisorption [109–111]. Also, based on the COHP analysis, strong agostic interactions between the C–H bonds of methyl and ethyl groups and the Pt sites of high symmetries were proposed for C–H bond activation [108]. This may find useful application in further delineating the mechanism of the formic acid oxidation reaction (FAOR) and MOR on metal (Pt) surfaces, where C–H bond-breaking is a necessary reaction step. This line of reasoning may also be useful in designing suitable catalysts for partial oxidation of methane.

Indeed, the aforementioned EOS description has long been embodied in the organometallic analogy of surface bonding advocated by Somorjai [112–114] and in the frontier-orbital formalism by Hoffmann [115, 116], which has been very successful in rationalizing many reaction mechanisms at solid/gas interfaces of heterogeneous catalysis. It is somewhat surprising that it has not found wide-spread use in electrocatalysis lately, which might have to do with the fact that the powerful valence-electron-orbital-probing ultraviolet photoelectron spectroscopy is not applicable to a solid/liquid interface, so a direct experimental connection with the

chemically intuitive EOS description is thus lost. Nonetheless, we strongly believe that an EOS description as briefly mentioned above can complement the highly successful d-band center theory by offering more chemical specificity in terms of surface-bonding-involved electronic orbitals by which the chemistry taking place at an EC interface may be better nuanced. Moreover, FAOR, MOR, and oxygen reduction reaction (ORR) at an electrode surface, all involve elementary reaction steps that will necessarily have Pt–H, Pt–O, Pt-CH$_3$, and/or Pt–CH$_2$ bond formation and C–H, O–H, and/or O=O bond breakings, either sequentially or simultaneously. They can thus serve as a natural and fertile testing ground for the EOS description. Therefore, the EOS description can help parse more insightfully the chemistry of M@Pt core-shell NPs for fuel cell electrocatalysis as a function of core element M at an electronic and molecular level.

Figure 5.11 illustrates some EOS information obtained by the ^{195}Pt and ^{13}CO NMR: the pure Pt has the highest s-like electrons at the Fermi level, Ru@Pt lowest, with Au@Pt in between. Now if higher availability of s-like electrons leads to stronger Pt-H bonding, the ability to abstract hydrogen would be strongest on Pt, weakest on Ru@Pt, with Au@Pt in between. For MOR, stronger hydrogen abstracting ability would lead to more generation of CO [117], which would rationalize why only very low amount of CO was observed on the Ru@Pt (Fig. 5.6b). At the same time, the availability of d-like electrons is not reduced at all as compared to pure Pt so it would retain its ability to bind oxygen-containing species, which would facilitate the formation of methoxy therefore enhance the direct reaction pathway [117]. In other words, the higher MOR activity on Ru@Pt
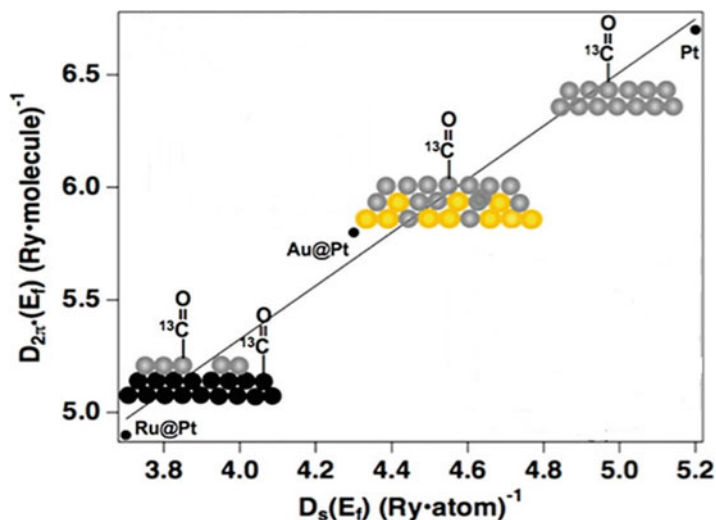

Fig. 5.11 Correlation between the $D_{2\pi^*}(E_f)$ and $D_s(E_f)$ deduced by using the two-band model from the ^{13}C NMR Data of CO$_{ads}$ on the Pt, Ru@Pt and Au@Pt NPs as well as ^{195}Pt NMR of them. Adapted from [71] with permission (© 2012 American Chemical Society)

might arise from its ability to enhance the direct reaction pathway for MOR. By the same token, the substantially reduced d-like electrons at the Fermi level for the Au@Pt would account for its inferior ability to do MOR because of its worsened ability to bond oxygen-containing species.

As to the blue shift of the Pt–CO vibration from the pure Pt to Ru@Pt observed by *in situ* EC-SERS, one could rationalize it by the reduction in *s*-like electrons at the Fermi level as this correlates to a lower $D_{2\pi*}(E_f)$ (Fig. 5.11), an indication of stronger Pt–CO bonding [105]. Consequently, $\nu_{Pt–CO}$ became higher on the Ru@Pt NPs.

5.7   Summary and Future Outlooks

We have shown in this chapter that integrating *in situ* EC NMR, SEIRAS and SERS studies of the Ru@Pt and Au@Pt NPs has enabled us to achieve a better mechanistic understanding of the two systems. *In situ* ^{195}Pt and ^{13}C NMR were able to provide some quantitative EOS information based on which some SEIRAS and SERS observations can be rationalized. The more relevant information one can garner, the better one can understand the catalyst's performance through which better performing electrocatalysts can be designed and developed. For instance, for Ru@Pt NPs, the SEIRAS data have suggested that segregated Pt and Ru ensembles seem to help enhance the MOR reactivity. Also, lowering the s-like but increasing the d-like electrons' availability may guide MOR through the direct reaction pathway without generating poisonous CO. Such specific information can be fed to the next round of designing and developing better MOR electrocatalysts.

In terms of developing further *in situ* techniques, there are several promising ones on the horizon that will become mature in the next decade. The first is the synchrotron light source and free-electron laser [118] based *in situ* X-ray spectroscopic methods [119]. As the synchrotron light source becomes more intense, the sensitivity of the technique will improve as well. It is also expected that the spatial resolution of X-ray based microscope and imaging will also improve substantially over the next decade. The second is the simple and straightforward high-resolution *in situ* EC NMR [120] that can explore all the analytical power of routine NMR. The third is nitrogen vacancy based scanning NMR microscope [121–123]. The key features of these new developments are chemical specificity, sensitivity, and spatial resolution.

References

1. Markovic NM, Ross PN (2000) New electrocatalysts for fuel cells from model surfaces to commercial catalysts. CATTECH 4:110–126
2. Steele BCH, Heinzel A (2001) Materials for fuel-cell technologies. Nature 414 (6861):345–352
3. Girishkumar G, McCloskey B, Luntz AC, Swanson S, Wilcke W (2010) Lithium–air battery: promise and challenges. J Phys Chem Lett 1(14):2193–2203. doi:10.1021/jz1005384
4. Shao Y, Park S, Xiao J, Zhang J-G, Wang Y, Liu J (2012) Electrocatalysts for nonaqueous lithium–air batteries: status, challenges, and perspective. ACS Catal 2(5):844–857. doi:10.1021/cs300036v
5. Zhang S, Yuan X-Z, Hin JNC, Wang H, Friedrich KA, Schulze M (2009) A review of platinum-based catalyst layer degradation in proton exchange membrane fuel cells. J Power Sources 194(2):588–600. http://dx.doi.org/10.1016/j.jpowsour.2009.06.073
6. Sealy C (2008) The problem with platinum. Mater Today 11(12):65–68
7. Arenz M, Mayrhofer KJJ, Stamenkovic V, Blizanac BB, Tomoyuki T, Ross PN, Markovic NM (2005) The effect of the particle size on the kinetics of CO electrooxidation on high surface area Pt catalysts. J Am Chem Soc 127(18):6819–6829. doi:10.1021/ja043602h
8. Lebedeva NP, Koper MTM, Feliu JM, van Santen RA (2002) Mechanism and kinetics of the electrochemical CO adlayer oxidation on Pt(111). J Electroanal Chem 524–525:242–251. http://dx.doi.org/10.1016/S0022-0728(02)00669-1
9. Iwasita T (2002) Electrocatalysis of methanol oxidation. Electrochim Acta 47:3663–3674
10. Wang H, Jusys Z, Behm RJ (2006) Ethanol electro-oxidation on carbon-supported Pt, PtRu and Pt_3Sn catalysts: a quantitative DEMS study. J Power Sources 154(2):351–359. http://dx.doi.org/10.1016/j.jpowsour.2005.10.034
11. Xia XH, Liess HD, Iwasita T (1997) Early stages in the oxidation of ethanol at low index single crystal platinum electrodes. J Electroanal Chem 437(1–2):233–240. http://dx.doi.org/10.1016/S0022-0728(97)00404-X
12. Kang Y, Qi L, Li M, Diaz RE, Su D, Adzic RR, Stach E, Li J, Murray CB (2012) Highly active Pt3Pb and core–shell Pt3Pb–Pt electrocatalysts for formic acid oxidation. ACS Nano 6 (3):2818–2825. doi:10.1021/nn3003373
13. Chen DJ, Zhou ZY, Wang Q, Xiang DM, Tian N, Sun SG (2010) A non-intermetallic PtPb/C catalyst of hollow structure with high activity and stability for electrooxidation of formic acid. Chem Commun 46(24):4252–4254. doi:10.1039/c002964e
14. Schmidt TJ, Ross Jr PN, Markovic NM (2002) Temperature dependent surface electrochemistry on Pt single crystals in alkaline electrolytes: Part 2. The hydrogen evolution/oxidation reaction. J Electroanal Chem 524–525:252–260. http://dx.doi.org/10.1016/S0022-0728(02)00683-6
15. Esposito DV, Hunt ST, Stottlemyer AL, Dobson KD, McCandless BE, Birkmire RW, Chen JG (2010) Low-cost hydrogen-evolution catalysts based on monolayer platinum on tungsten monocarbide substrates. Angew Chem Int Ed 49(51):9859–9862. doi:10.1002/anie.201004718
16. Lim B, Jiang M, Camargo PHC, Cho EC, Tao J, Lu X, Zhu Y, Xia Y (2009) Pd-Pt bimetallic nanodendrites with high activity for oxygen reduction. Science 324(5932):1302–1305. doi:10.1126/science.1170377
17. Zhang J, Sasaki K, Sutter E, Adzic RR (2007) Stabilization of platinum oxygen-reduction electrocatalysts using gold clusters. Science 315(5809):220–222
18. Lu YC, Xu ZC, Gasteiger HA, Chen S, Hamad-Schifferli K, Shao-Horn Y (2010) Platinum-gold nanoparticles: a highly active bifunctional electrocatalyst for rechargeable lithium-air batteries. J Am Chem Soc 132(35):12170–12171. doi:10.1021/ja1036572
19. Kerbach I, Climent V, Feliu JM (2011) Reduction of CO_2 on bismuth modified Pt(110) single-crystal surfaces. Effect of bismuth and poisoning intermediates on the rate of hydrogen

evolution. Electrochim Acta 56(12):4451–4456. http://dx.doi.org/10.1016/j.electacta.2011.02.027

20. Qu J, Zhang X, Wang Y, Xie C (2005) Electrochemical reduction of CO_2 on RuO_2/TiO_2 nanotubes composite modified Pt electrode. Electrochim Acta 50(16–17):3576–3580. http://dx.doi.org/10.1016/j.electacta.2004.11.061

21. Climent V, Garcia-Araez N, Feliu JM (2009) Clues for the molecular-level understanding of electrocatalysis on single-crystal platinum surfaces modified by p-block adatoms. Fuel cell catalysis a surface science approach. Wiley, Hoboken

22. Liu P, Nørskov JK (2001) Ligand and ensemble effects in adsorption on alloy surfaces. Phys Chem Chem Phys 3(17):3814–3818. doi:10.1039/b103525h

23. Tong YY, Wieckowski A, Oldfield E (2002) NMR of electrocatalysts. J Phys Chem B 106(10):2434–2446. doi:10.1021/jp0129939

24. Du B, Danberry AL, Park I-S, Sung Y-E, Tong Y (2008) Spatially resolved [195]Pt NMR of carbon-supported PtRu electrocatalysts: local electronic properties, elemental composition, and catalytic activity. J Chem Phys 128(5):052311. doi:10.1063/1.2830952

25. Tan F, Du B, Danberry AL, Park I-S, Sung Y-E, Tong Y (2008) A comparative in situ 195Pt electrochemical-NMR investigation of PtRu nanoparticles supported on diverse carbon nanomaterials. Faraday Discuss 140:139–153. doi:10.1039/b803073a

26. Tong RC, Wieckowski A, Oldfield E (2000) A detailed NMR-based model for CO on Pt catalysts in an electrochemical environment: shifts, relaxation, back-bonding, and the fermi-level local density of states. J Am Chem Soc 122(6):1123–1129. doi:10.1021/ja9922274

27. Tong KHS, Babu PK, Waszczuk P, Wieckowski A, Oldfield E (2002) An NMR investigation of CO tolerance in a Pt/Ru fuel cell catalyst. J Am Chem Soc 124(3):468–473. doi:10.1021/ja011729q

28. Kobayashi T, Babu PK, Gancs L, Chung JH, Oldfield E, Wieckowski A (2005) An NMR determination of CO diffusion on platinum electrocatalysts. J Am Chem Soc 127(41):14164–14165. doi:10.1021/ja0550475

29. Tian ZQ, Ren B (2004) Adsorption and reaction at electrochemical interfaces as probed by surface-enhanced Raman spectroscopy. Annu Rev Phys Chem 55:197–229. doi:10.1146/annurev.physchem.54.011002.103833

30. Osawa M (2006) Diffraction and spectroscopic methods in electrochemistry: in-situ surface-enhanced infrared spectroscopy of the electrode/solution interface, vol 9, Advances in electrochemical science and engineering. Wiley-VCH, New York

31. Osawa M, Ataka K, Yoshii K, Yotsuyanagi T (1993) Surface-enhanced infrared ATR spectroscopy for in situ studies of electrode/electrolyte interfaces. J Electron Spectrosc Relat Phenom 64:371–379. uuid: CE0FC3F0-7DA6-4A00-8375-39A57E55959A

32. Ataka K, Yotsuyanagi T, Osawa M (1996) Potential-dependent reorientation of water molecules at an electrode/electrolyte interface studied by surface-enhanced infrared absorption spectroscopy. J Phys Chem 100(25):10664–10672. doi:10.1021/jp953636z

33. Garcia-Araez N, Rodriguez P, Bakker HJ, Koper MTM (2012) Effect of the surface structure of gold electrodes on the coadsorption of water and anions. J Phys Chem C 116(7):4786–4792. doi:10.1021/jp211782v

34. Sun SG, Cai WB, Wan LJ, Osawa M (1999) Infrared absorption enhancement for CO adsorbed on Au films in perchloric acid solutions and effects of surface structure studied by cyclic voltammetry, scanning tunneling microscopy, and surface-enhanced IR spectroscopy. J Phys Chem B 103(13):2460–2466

35. Yoshida M, Yamakata A, Takanabe K, Kubota J, Osawa M, Domen K (2009) ATR-SEIRAS investigation of the fermi level of Pt cocatalyst on a GaN photocatalyst for hydrogen evolution under irradiation. J Am Chem Soc 131(37):13218–13219. doi:10.1021/ja904991p

36. Shao MH, Adzic RR (2005) Electrooxidation of ethanol on a Pt electrode in acid solutions: in situ ATR-SEIRAS study. Electrochim Acta 50(12):2415–2422. doi:10.1016/j.electacta.2004.10.063

37. Smolinka T, Heinen M, Chen YX, Jusys Z, Lehnert W, Behm RJ (2005) CO_2 reduction on Pt electrocatalysts and its impact on H-2 oxidation in CO_2 containing fuel cell feed gas—a combined in situ infrared spectroscopy, mass spectrometry and fuel cell performance study. Electrochim Acta 50(25–26):5189–5199. doi:10.1016/j.electacta.2005.02.082

38. Kunimatsu K, Uchida H, Osawa M, Watanabe M (2006) In situ infrared spectroscopic and electrochemical study of hydrogen electro-oxidation on Pt electrode in sulfuric acid. J Electroanal Chem 587(2):299–307. doi:10.1016/j.jelechem.2005.11.026

39. Osawa M, K-i K, Samjeské G, Uchida T, Ikeshoji T, Cuesta A, Gutiérrez C (2011) The role of bridge-bonded adsorbed formate in the electrocatalytic oxidation of formic acid on platinum. Angew Chem Int Ed 50(5):1159–1163. doi:10.1002/anie.201004782

40. Chen YX, Miki A, Ye S, Sakai H, Osawa M (2003) Formate, an active intermediate for direct oxidation of methanol on Pt electrode. J Am Chem Soc 125(13):3680–3681. doi:10.1021/ja029044t

41. Samjeske G, Komatsu K, Osawa M (2009) Dynamics of CO oxidation on a polycrystalline platinum electrode: a time-resolved infrared study. J Phys Chem C 113(23):10222–10228. doi:10.1021/jp900582c

42. Kunimatsu K, Hanawa H, Uchida H, Watanabe M (2009) Role of adsorbed species in methanol oxidation on Pt studied by ATR-FTIRAS combined with linear potential sweep voltammetry. J Electroanal Chem 632(1–2):109–119

43. Yajima T, Uchida H, Watanabe M (2004) In-situ ATR-FTIR spectroscopic study of electro-oxidation of methanol and adsorbed CO at PtRu alloy. J Phys Chem B 108(8):2654–2659. doi:10.1021/jp037215q

44. Wang C, Peng B, Xie H-N, Zhang H-X, Shi F-F, Cai W-B (2009) Facile fabrication of Pt, Pd and Pt–Pd alloy films on Si with tunable infrared internal reflection absorption and synergetic electrocatalysis. J Phys Chem C 113(31):13841–13846. doi:10.1021/jp9034562

45. Miyake H, Okada T, Samjeske G, Osawa M (2008) Formic acid electrooxidation on Pd in acidic solutions studied by surface-enhanced infrared absorption spectroscopy. Phys Chem Chem Phys 10(25):3662–3669. doi:10.1039/b805955a

46. Wang HF, Yan YG, Hu SJ, Cai WB, Xu QH, Osawa M (2007) Seeded growth fabrication of Cu-on-Si electrodes for in situ ATR-SEIRAS applications. Electrochim Acta 52(19):5950–5957. doi:10.1016/j.electacta.2007.03.042

47. Delgado JM, Orts JM, Rodes A (2007) A comparison between chemical and sputtering methods for preparing thin-film silver electrodes for in situ ATR-SEIRAS studies. Electrochim Acta 52(14):4605–4613. doi:10.1016/j.electacta.2006.12.045

48. Yajima T, Wakabayashi N, Uchida H, Watanabe M (2003) Adsorbed water for the electro-oxidation of methanol at Pt-Ru alloy. Chem Commun 7:828–829. doi:10.1039/b212197b

49. Yan LQ-X, Huo S-J, Ma M, Cai W-B, Osawa M (2005) Ubiquitous strategy for probing ATR surface-enhanced infrared absorption at platinum group metal-electrolyte interfaces. J Phys Chem B 109(16):7900–7906. doi:10.1021/jp044085s

50. Wang J-Y, Zhang H-X, Jiang K, Cai W-B (2011) From HCOOH to CO at Pd electrodes: a surface-enhanced infrared spectroscopy study. J Am Chem Soc 133:14876–14879. doi:10.1021/ja205747j

51. Vassilev P, Koper MTM (2007) Electrochemical reduction of oxygen on gold surfaces: a density functional theory study of intermediates and reaction paths. J Phys Chem C 111(6):2607–2613. doi:10.1021/jp064515+

52. Kunimatsu K, Yoda T, Tryk DA, Uchida H, Watanabe M (2010) In situ ATR-FTIR study of oxygen reduction at the Pt/Nafion interface. Phys Chem Chem Phys 12(3):621–629. doi:10.1039/B917306D

53. Cuesta A, Cabello G, Hartl FW, Escudero-Escribano M, Vaz-Domínguez C, Kibler LA, Osawa M, Gutiérrez C (2013) Electrooxidation of formic acid on gold: an ATR-SEIRAS study of the role of adsorbed formate. Catal Today 202:79–86. http://dx.doi.org/10.1016/j.cattod.2012.04.022

54. Shiroishi H, Ayato Y, Kunimatsu K, Okada T (2005) Study of adsorbed water on Pt during methanol oxidation by ATR-SEIRAS (surface-enhanced infrared absorption spectroscopy). J Electroanal Chem 581(1):132–138. doi:10.1016/j.jelechem.2005.04.027

55. Futamata M, Luo LQ (2007) Adsorbed water and CO on Pt electrode modified with Ru. J Power Sources 164(2):532–537. doi:10.1016/j.jpowsour.2006.10.079

56. Li X, Gewirth AA (2005) Oxygen electroreduction through a superoxide intermediate on Bi-modified Au surfaces. J Am Chem Soc 127(14):5252–5260. doi:10.1021/ja043170a

57. Yang H, Yang Y, Zou S (2007) In situ surface-enhanced raman spectroscopic studies of CO adsorption and methanol oxidation on Ru-modified Pt surfaces. J Phys Chem C 111 (51):19058–19065. doi:10.1021/jp075929l

58. Xu B, Park I-S, Li Y, Chen D-J, Tong YJ (2011) An in situ SERS investigation of the chemical states of sulfur species adsorbed onto Pt from different sulfur sources. J Electroanal Chem 662:52–56. doi:10.1016/j.jelechem.2011.02.031

59. Tian ZQ, Ren B, Wu DY (2002) Surface-enhanced Raman scattering: from noble to transition metals and from rough surfaces to ordered nanostructures. J Phys Chem B 106 (37):9463–9483. doi:10.1021/jp0257449

60. Gómez R, Pérez JM, Solla-Gullón J, Montiel V, Aldaz A (2004) In situ surface enhanced raman spectroscopy on electrodes with platinum and palladium nanoparticle ensembles. J Phys Chem B 108(28):9943–9949. doi:10.1021/jp038030m

61. Gómez R, Solla-Gullón J, Pérez JM, Aldaz A (2005) Surface-enhanced raman spectroscopy study of ethylene adsorbed on a Pt electrode decorated with Pt nanoparticles. ChemPhysChem 6(10):2017–2021. doi:10.1002/cphc.200500168

62. Solla-Gullón J, Gómez R, Aldaz A, Pérez JM (2008) A combination of SERS and electro-chemistry in Pt nanoparticle electrocatalysis: promotion of formic acid oxidation by ethylidyne. Eletrochem Commun 10(2):319–322. http://dx.doi.org/10.1016/j.elecom.2007.12.010

63. Pu Zhang JC, Chen Y-X, Tang Z-Q, Dong C, Yang JL, Wu D-Y, Ren B, Tian Z-Q (2010) Potential-dependent chemisorption of carbon monoxide at a gold core-platinum shell nano-particle electrode: a combined study by electrochemical in situ surface-enhanced raman spectroscopy and density functional theory. J Phys Chem C 114:403–411

64. Park I-S, Chen D-J, Atienza DO, Tong YYJ (2013) Enhanced CO monolayer electro-oxidation reaction on sulfide-adsorbed Pt nanoparticles: a combined electrochemical and in situ ATR-SEIRAS spectroscopic study. Catal Today 202:175–182. http://dx.doi.org/10.1016/j.cattod.2012.05.045

65. Park I-S, Atienza DO, Hofstead-Duffy AM, Chen D, Tong YJ (2011) Mechanistic insights on sulfide-adsorption enhanced activity of methanol electro-oxidation on Pt nanoparticles. ACS Catal 2(1):168–174. doi:10.1021/cs200546f

66. Li X, Gewirth AA (2003) Peroxide electroreduction on bi-modified au surfaces: vibrational spectroscopy and density functional calculations. J Am Chem Soc 125(23):7086–7099. doi:10.1021/ja034125q

67. Li X, Heryadi D, Gewirth AA (2005) Electroreduction activity of hydrogen peroxide on Pt and Au electrodes. Langmuir 21(20):9251–9259. doi:10.1021/la0508745

68. Du B, Rabb SA, Zangmeister C, Tong Y (2009) A volcano curve: optimizing methanol electro-oxidation on Pt-decorated Ru nanoparticles. Phys Chem Chem Phys 11 (37):8231–8239. uuid:F4A2892D-47E4-478B-825C-8EB0584C7F0F

69. Le Rhun V, Garnier E, Pronier S, Alonso-Vante N (2000) Electrocatalysis on nanoscale ruthenium-based material manufactured by carbonyl decomposition. Electrochem Commun 2(7):475–479

70. Park IS, Lee KS, Jung DS, Park HY, Sung Y-E (2007) Electrocatalytic activity of carbon-supported Pt-Au nanoparticles for methanol electro-oxidation. Electrochim Acta 52:5599–5605. uuid:84E52FA9-41B4-4917-93F1-E2222D793214

71. Atienza DO, Allison TC, Tong YJ (2012) Spatially resolved electronic alterations as seen by in situ 195Pt and 13CO NMR in Ru@Pt and Au@Pt core–shell nanoparticles. J Phys Chem C 116(50):26480–26486. doi:10.1021/jp310313k

72. Du B, Zaluzhna O, Tong YJ (2011) Electrocatalytic properties of Au@Pt nanoparticles: effects of Pt shell packing density and Au core size. Phys Chem Chem Phys 13 (24):11568–11574

73. Tong RC, Godbout N, Wieckowski A, Oldfield E (1999) Correlation between the knight shift of chemisorbed CO and the fermi level local density of states at clean platinum catalyst surfaces. J Am Chem Soc 121(13):2996–3003. doi:10.1021/ja9830492

74. Stokes HT, Rhodes HE, Wang PK, Slichter CP, Sinfelt JH (1982) NMR of platinum catalysts. III. Microscopic variation of the Knight shifts. Phys Rev B 26(7):3575–3581. uuid:572642F8-60BF-49D7-83A6-B7AE0A58B890

75. Bucher J, van der Klink J (1988) Electronic properties of small supported Pt particles: NMR study of 195Pt hyperfine parameters. Phys Rev B Condens Matter 38(16):11038–11047. doi:10.1103/PhysRevB.38.11038

76. Adekunle AS, Ozoemena KI (2008) Electron transfer behaviour of single-walled carbon nanotubes electro-decorated with nickel and nickel oxide layers. Electrochim Acta 53 (19):5774–5782

77. Wang PK, Ansermet JP, Rudaz SL, Wang Z, Shore S, Slichter CP, Sinfelt JH (1986) NMR studies of simple molecules on metal surfaces. Science 234(4772):35–41. doi:10.1126/science.234.4772.35

78. Korringa J (1950) Nuclear magnetic relaxation and resonance line shift in metals. Physica XVI(7–8):601–610

79. Blyholder G (1964) Molecular orbital view of chemisorbed carbon monoxide. J Phys Chem 68(10):2772–2777. doi:10.1021/j100792a006

80. Chen D-J, Hofstead-Duffy AM, Park I-S, Atienza DO, Susut C, Sun S-G, Tong YJ (2011) Identification of the most active sites and surface water species: a comparative study of CO and methanol oxidation reactions on core–shell M@Pt (M = Ru, Au) nanoparticles by in situ IR spectroscopy. J Phys Chem C 115(17):8735–8743. doi:10.1021/jp200557m

81. Chen D-J, Xu B, Sun S-G, Tong YJ (2012) Electroless deposition of ultrathin Au film for surface enhanced in situ spectroelectrochemistry and reaction-driven surface reconstruction for oxygen reduction reaction. Catal Today 182:46–53. doi:10.1016/j.cattod.2011.08.052

82. Lin WF, Zei MS, Eiswirth M, Ertl G, Iwasita T, Vielstich W (1999) Electrocatalytic Activity of Ru-Modified Pt(111) Electrodes toward CO Oxidation. J Phys Chem B 103 (33):6968–6977. doi:10.1021/jp9910901

83. Lu GQ, White JO, Wieckowski A (2004) Vibrational analysis of chemisorbed CO on the Pt (111)/Ru bimetallic electrode. Surf Sci 564(1–3):131–140

84. Spendelow JS, Babu PK, Wieckowski A (2005) Electrocatalytic oxidation of carbon monoxide and methanol on platinum surfaces decorated with ruthenium. Curr Opin Solid State Mater Sci 9(1–2):37–48

85. Watanabe M, Sato T, Kunimatsu K, Uchida H (2008) Temperature dependence of co-adsorption of carbon monoxide and water on highly dispersed Pt/C and PtRu/C electrodes studied by in-situ ATR-FTIRAS. Electrochim Acta 53(23):6928–6937. doi:10.1016/j.electacta.2008.02.023

86. Ianniello R, Schmidt VM, Stimming U, Stumper J, Wallau A (1994) CO adsorption and oxidation on Pt and Pt Ru alloys: dependence on substrate composition. Electrochim Acta 39 (11–12):1863–1869

87. Friedrich KA, Geyzers KP, Dickinson AJ, Stimming U (2002) Fundamental aspects in electrocatalysis: from the reactivity of single-crystals to fuel cell electrocatalysts. J Electroanal Chem 524–525:261–272

88. Zheng MS, Sun SG, Chen SP (2001) Abnormal infrared effects and electrocatalytic properties of nanometer scale thin film of PtRu alloys for CO adsorption and oxidation. J Appl Electrochem 31(7):749–757

89. Lin WF, Iwasita T, Vielstich W (1999) Catalysis of CO electrooxidation at Pt, Ru, and PtRu alloy. An in situ FTIR study. J Phys Chem B 103(16):3250–3257

90. Brankovic SR, Wang JX, Adzic RR (2001) Pt submonolayers on Ru nanoparticles—a novel low Pt loading, high CO tolerance fuel cell electrocatalyst. Electrochem Solid State Lett 4 (12):A217–a220

91. Vogel W, Le Rhun V, Garnier E, Alonso-Vante N (2001) Ru clusters synthesized chemically from dissolved carbonyl: in situ study of a novel electrocatalyst in the gas phase and in electrochemical environment. J Phys Chem B 105(22):5238–5243. doi:10.1021/jp0100654

92. Chen DJ, Tong YYJ (2015) In situ Raman spectroscopic measurement of near-surface proton concentration changes during electrochemical reactions. Chem Commun 51(26):5683–5686. doi:10.1039/C5CC00427F

93. Zhu Y, Uchida H, Watanabe M (1999) Oxidation of carbon monoxide at a platinum film electrode studied by Fourier transform infrared spectroscopy with attenuated total reflection technique. Langmuir 15(25):8757–8764. doi:10.1021/la990835r

94. Peremans A, Tadjeddine A (1994) Vibrational spectroscopy of electrochemically deposited hydrogen on platinum. Phys Rev Lett 73(22):3010

95. Osawa M, Tsushima M, Mogami H, Samjeske G, Yamakata A (2008) Structure of water at the electrified platinum-water interface: a study by surface-enhanced infrared absorption spectroscopy. J Phys Chem C 112(11):4248–4256. doi:10.1021/jp710386g

96. Kunimatsu K, Senzaki T, Samjesk G, Tsushima M, Osawa M (2007) Hydrogen adsorption and hydrogen evolution reaction on a polycrystalline Pt electrode studied by surface-enhanced infrared absorption spectroscopy. Electrochim Acta 52(18):5715–5724

97. Kunimatsu K, Uchida H, Osawa M, Watanabe M (2006) In situ infrared spectroscopic and electrochemical study of hydrogen electro-oxidation on Pt electrode in sulfuric acid (vol 587, p 299, 2006). J Electroanal Chem 596(2):169–169. doi:10.1016/j.jelechem.2006.07.015

98. Futamata M, Luo L, Nishihara C (2005) ATR-SEIR study of anions and water adsorbed on platinum electrode. Surf Sci 590(2–3):196–211

99. Climent V, Gomez R, Feliu JM (1999) Effect of increasing amount of steps on the potential of zero total charge of Pt(111) electrodes. Electrochim Acta 45(4–5):629–637

100. Bergelin M, Herrero E, Feliu JM, Wasberg M (1999) Oxidation of CO adlayers on Pt(111) at low potentials: an impinging jet study in H_2SO_4 electrolyte with mathematical modeling of the current transients. J Electroanal Chem 467(1–2):74–84

101. Vidal-Iglesias FJ, Solla-Gullon J, Campina JM, Herrero E, Aldaz A, Feliu JM (2009) CO monolayer oxidation on stepped Pt(S) [(n-1)(100)*(110)] surfaces. Electrochim Acta 54 (19):4459–4466

102. Roth C, Benker N, Buhrmester T, Mazurek M, Loster M, Fuess H, Koningsberger DC, Ramaker DE (2005) Determination of O[H] and CO coverage and adsorption sites on PtRu electrodes in an operating PEM fuel cell. J Am Chem Soc 127(42):14607–14615. doi:10.1021/ja050139f

103. Coker DF, Miller RE, Watts RO (1985) The infrared predissociation spectra of water clusters. J Chem Phys 82(8):3554–3562

104. Richmond GL (2002) Molecular bonding and interactions at aqueous surfaces as probed by vibrational sum frequency spectroscopy. Chem Rev 102(8):2693–2724. doi:10.1021/cr0006876

105. Wasileski SA, Koper MTM, Weaver MJ (2001) Field-dependent chemisorption of carbon monoxide on platinum-group (111) surfaces: relationships between binding energetics, geometries, and vibrational properties as assessed by density functional theory. J Phys Chem B 105(17):3518–3530. doi:10.1021/jp003263o

106. Oudenhuijzen MK, van Bokhoven JA, Ramaker DE, Koningsberger DC (2004) Theoretical study on Pt particle adsorbate bonding: influence of support ionicity and implications for catalysis. J Phys Chem B 108(52):20247–20254. uuid:FEE96E5D-8FA4-4172-95A9-A6C6AC66EE05

107. Dronskowski R, Bloechl PE (1993) Crystal orbital Hamilton populations (COHP): energy-resolved visualization of chemical bonding in solids based on density-functional calculations. J Phys Chem 97(33):8617–8624. doi:10.1021/j100135a014

108. Papoian G, Norskov JK, Hoffmann R (2000) A comparative theoretical study of the hydrogen, methyl, and ethyl chemisorption on the Pt(111) surface. J Am Chem Soc 122 (17):4129–4144. doi:10.1021/ja993483j

109. Glassey WV, Hoffmann R (2001) A comparative study of the p (2×2)-CO/M (111), M = Pt, Cu, Al chemisorption systems. J Phys Chem B 105(16):3245–3260. doi:10.1021/jp003922x

110. Glassey WV, Hoffmann R (2001) A molecular orbital study of surface–adsorbate interactions during the oxidation of CO on the Pt(111) surface. Surf Sci 475(1–3):47–60. doi:10.1016/S0039-6028(00)01062-1

111. Glassey WV, Papoian GA, Hoffmann R (1999) Total energy partitioning within a one-electron formalism: a Hamilton population study of surface–CO interaction in the c (2×2)-CO/ Ni(100) chemisorption system. J Chem Phys 111(3):893–910. doi:10.1063/1.479200

112. Somorjai GA, Aliaga C (2010) Molecular studies of model surfaces of metals from single crystals to nanoparticles under catalytic reaction conditions. Evolution from prenatal and postmortem studies of catalysts. Langmuir 26(21):16190–16203. doi:10.1021/la101884s

113. Somorjai GA, Contreras AM, Montano M, Rioux RM (2006) Clusters, surfaces, and catalysis. Proc Natl Acad Sci U S A 103:10577–10583

114. Somorjai GA (1994) Introduction to surface chemistry and catalysis. Wiley, New York

115. Hoffmann R (1993) A chemical and theoretical approach to bonding at surfaces. J Phys Condens Matter 5:A1–A16

116. Hoffmann R (1971) Interaction of orbitals through space and through bonds. Acc Chem Res 4 (1):1–9

117. Housmans THM, Wonders AH, Koper MTM (2006) Structure sensitivity of methanol electrooxidation pathways on platinum: an on-line electrochemical mass spectrometry study. J Phys Chem B 110(20):10021–10031. doi:10.1021/jp055949s

118. Huang Z, Kim K-J (2007) Review of X-ray free-electron laser theory. Phys Rev ST Accel Beams 10(3):034801–034826. doi:10.1103/PhysRevSTAB.10.034801

119. Shearing P, Wu Y, Harris SJ, Brandon N (2011) In situ X-ray spectroscopy and imaging of battery materials. Interface 20:43–47. uuid:27465B6F-DD87-45E1-8587-699AFDB658FF

120. Huang L, Sorte EG, Sun SG, Tong YYJ (2015) A straightforward implementation of in situ solution electrochemical 13C NMR spectroscopy for studying reactions on commercial electrocatalysts: ethanol oxidation. Chem Commun 51(38):1–3. doi:10.1039/C5CC00862J

121. DeVience SJ, Pham LM, Lovchinsky I, Sushkov AO, Bar-Gill N, Belthangady C, Casola F, Corbett M, Zhang H, Lukin M, Park H, Yacoby A, Walsworth RL (2015) Nanoscale NMR spectroscopy and imaging of multiple nuclear species. Nat Nanotechnol 10(2):129–134. doi:10.1038/nnano.2014.313

122. Häberle T, Schmid-Lorch D, Reinhard F, Wrachtrup J (2015) Nanoscale nuclear magnetic imaging with chemical contrast. Nat Nanotechnol 10(2):125–128. doi:10.1038/nnano.2014.299

123. Rugar D, Mamin HJ, Sherwood MH, Kim M, Rettner CT, Ohno K, Awschalom DD (2015) Proton magnetic resonance imaging using a nitrogen-vacancy spin sensor. Nat Nanotechnol 10(2):120–124. doi:10.1038/nnano.2014.288